Liquid Crystals Reviews
Publication details, including instructions for authors and subscription information:
http://www.tandfonline.com/loi/tlcr20

Single-photon experiments with liquid crystals for quantum science and quantum engineering applications

Svetlana G. Lukishova[a], Andreas C. Liapis[a], Luke J. Bissell[b], George M. Gehring[a] & Robert W. Boyd[acd]

[a] The Institute of Optics, University of Rochester, Rochester, NY 14627, USA

[b] Air Force Research Laboratory, Wright-Patterson Air Force Base, OH 45433, USA

[c] Department of Physics and Astronomy, University of Rochester, Rochester, NY 14627, USA

[d] Department of Physics and School of Electrical Engineering and Computer Science, University of Ottawa, Ottawa, ON K1N 6N5, Canada

Accepted author version posted online: 14 Aug 2014.Published online: 26 Sep 2014.

To cite this article: Svetlana G. Lukishova, Andreas C. Liapis, Luke J. Bissell, George M. Gehring & Robert W. Boyd (2014) Single-photon experiments with liquid crystals for quantum science and quantum engineering applications, Liquid Crystals Reviews, 2:2, 111-129, DOI: 10.1080/21680396.2014.954015

To link to this article: http://dx.doi.org/10.1080/21680396.2014.954015

Liquid Crystals Reviews, 2014
Vol. 2, No. 2, 111–129, http://dx.doi.org/10.1080/21680396.2014.954015

Taylor & Francis
Taylor & Francis Group

Single-photon experiments with liquid crystals for quantum science and quantum engineering applications

Svetlana G. Lukishova[a*], Andreas C. Liapis[a], Luke J. Bissell[b], George M. Gehring[a], and Robert W. Boyd[a,c,d]

[a]*The Institute of Optics, University of Rochester, Rochester, NY 14627, USA;* [b]*Air Force Research Laboratory, Wright-Patterson Air Force Base, OH 45433, USA;* [c]*Department of Physics and Astronomy, University of Rochester, Rochester, NY 14627, USA;* [d]*Department of Physics and School of Electrical Engineering and Computer Science, University of Ottawa, Ottawa, ON K1N 6N5, Canada*

(*Received 30 June 2014; accepted 8 August 2014*)

We present here our results on using liquid crystals (LCs) in experiments with nonclassical light sources: (1) single-photon sources exhibiting antibunching (separation of all photons in time), which are key components for secure quantum communication systems and (2) entangled photon source with photons exhibiting quantum interference in a Hong–Ou–Mandel interferometer. In the first part, both nematic and cholesteric liquid crystal (CLC) hosts were used to create *definite linear* or *circular polarization* of antibunched photons emitted by different types of single emitters (dye molecules, nanocrystal quantum dots (NQDs), nanodiamonds with color centers, etc.). If the photon has unknown polarization, filtering it through a polarizer to produce the desired polarization for quantum key distribution with bits based on polarization states of photons will reduce by half the efficiency of a quantum cryptography system. In the first part, we also provide our results on observation of a circular polarized microcavity resonance in NQD fluorescence in a 1-D chiral photonic bandgap CLC microcavity. In the second part of this paper with indistinguishable, time-entangled photons, we demonstrate our experimental results on simulating quantum mechanical barrier tunneling phenomena. A Hong–Ou–Mandel dip (quantum interference effect) is shifted when a phase change was introduced on the way of one of entangled photons in pair (one arm of the interferometer) by inserting in this arm an electrically controlled planar-aligned nematic LC layer between two prisms in the conditions close to a frustrated total internal reflection. By applying different AC-voltages to the planar-aligned nematic layer and changing its refractive index, we can obtain various conditions for incident photon propagation – from total reflection to total transmission. Measuring changes of tunneling times of photon through this structure with femtosecond resolution permitted us to answer some unresolved questions in quantum mechanical barrier tunneling phenomena.

Keywords: polarized single-photon source; antibunching; nanocrystal quantum dots; nitrogen vacancy color centers in nanodiamonds; nematic; cholesteric liquid crystals; Hong–Ou–Mandel interferometer; entangled photons; quantum mechanical barrier tunneling time; double-prism structure; frustrated total internal reflection

1. Introduction

Thermotropic liquid crystal (LC) materials and devices have found many new applications in photonics beyond well-developed display technology, waveplates, optical filters, and spatial light modulators. In addition to high-power applications of LCs in laser optics,[1–6] optical power limiters,[7,8] and cholesteric lasers,[9–17] some recent new photonics applications of LCs are phase plates with singularities (including q-plates with inhomogenous patterned distribution of the local optical axis in the transverse plane) [18–24] and nanophotonics.[25–27] The purpose of this paper is to familiarize the reader with some applications of LCs in quantum science and quantum engineering using as examples the experiments and methods developed at the Institute of Optics, University of Rochester.[28–42] Quantum optical applications of LCs, mostly connected with angular momentum of light and its manipulation using q-plates, were also reported by Italian groups.[18–21,23,24,43,44]

In two main parts of the present paper (Sections 2 and 3), we describe two directions developed in Rochester of using LC technology with nonclassical photon sources. Here we will briefly outline the main concepts of quantum optics which we are using in this review, as well as advantages of employing LC materials in very important, "hot topic" applications in quantum science and quantum engineering. It is important to emphasize that these experiments were carried out at low light levels, so photon counting techniques were used in all experiments.

1.1. *Single (antibunched)-photon sources operating at room temperatures*

The first part (Section 2) of this paper is an overview of the main results of our more than 10 years research on using planar-aligned monomeric or oligomeric cholesteric and nematic LCs for efficiently producing single photons with *definite circular* and *linear polarizations*.[28–34,36–39]

*Corresponding author. Emails: sluk@lle.rochester.edu, lukishova@hotmail.com

Single-photon source (SPS) is a nonclassical light source with *all* photons separated in time.[45–52] In common light sources (bulbs and sun light) and in lasers, such separation (antibunching) [53] cannot be obtained: multiple (nonseparated) photons cannot be avoided even in very faint sources (Figure 1). Figure 2 shows histograms of a probability to have different photon numbers when the mean photon number $\bar{n} = 1$ for various types of photon sources (antibunched, coherent (laser), and thermal).[54] For photon antibunching, the second-order coherence function $g^{(2)}(t) = \langle I(t)I(t+\tau)\rangle/\langle I(\tau)\rangle^2$ [55] should have a minimum at interphoton time $t = 0$. In an ideal case, $g^{(2)}(0) = 0$, indicating the absence of photon pairs. In this case also $g^{(2)}(t) \leq 1$. Here $I(t)$ is intensity and averaging is time averaging. For coherent (laser) light $g^{(2)}(t) = 1$ at any t, and for thermal light $g^{(2)}(0) = 2$ and $g^{(2)}(t) \geq 1$. Figure 3 illustrates dependences of $g^{(2)}(t)$ for sources with different photon statistics.

Using *all* photon separation, absolutely secure quantum communication (Figure 4) [56,57] will prevent any potential eavesdropper (Eve) from intercepting a message without the sender (Alice) and receiver (Bob) noticing. Bits of transferred information are coded in the photon polarization state. If the source emits more than one photon at a time, it would be possible for Eve to extract one of these photons without disturbing the other photon which would reveal Eve's presence. In the BB84 quantum key distribution protocol,[56] the sender (Alice) and receiver (Bob) employ the linear and circular polarization states of single photons. The linear and circular polarization bases can be used to provide two different

Figure 1. Photon separation in time for sources with different photon statistics: top (red) – single photons (antibunching); center (green) – thermal light (bunching); and bottom (yellow) – coherent (laser) light.

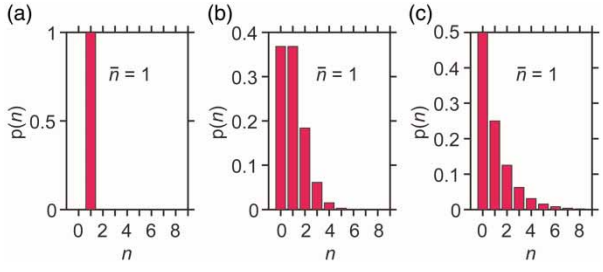

Figure 2. Photon number (n) probability distribution [$P(n)$] for photon sources with different statistics, but with the same mean photon number $\bar{n} = 1$. (a) Single (antibunched) photon source (Fock state); (b) laser (coherent) light; and (c) thermal source.

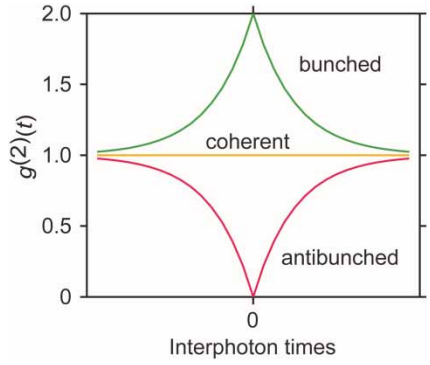

Figure 3. Dependence of a second-order coherence function $g^{(2)}(t)$ on an interphoton time t for light sources with different photon statistics.

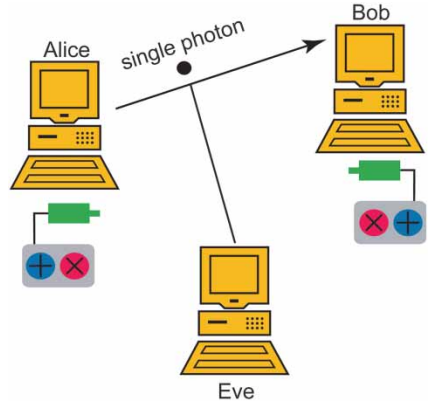

Figure 4. Quantum key distribution using single photons.

quantum-level representations of 0 and 1. So a desirable feature for a SPS is definite photon polarization, since, if the photon has unknown polarization, *filtering it through a polarizer* to produce the desired polarization for quantum key distribution *will reduce by half* the efficiency of a quantum cryptography system. The security of a system based on single photons will not be broken even if extremely powerful quantum computers come into existence, which will break the security of all currently secure systems, including all bank accounts, internet transactions, and military services. In May 2013, it was announced that a collaboration between NASA, Google, and the Universities Space Research Association launched a Quantum Artificial Intelligence Lab based on the D-Wave Two, the second commercially available, 512-bit quantum computer (as it was claimed) of D-Wave based on a superconducting processor.[58] Although there is no evidence yet that quantum speedup may take place with this particular model,[59] the research in this direction attracts the best minds in the world. In another implementation of quantum computers, it was suggested to use a SPS as the key hardware component of such a computer with linear optical elements and photodetectors.[60] In addition, single photons are very important in quantum metrology and in

fundamental physics experiments, for instance, in interference from uncoupled light sources and entanglement-state generation, in shedding light on wave–particle duality as well as fundamental issues of quantum measurement and uncertainty.

The critical issue in producing single photons exhibiting antibunching is the very low concentration of photon emitters dispersed in a host (less than 1 emitter/μm^3), such that, within an excitation laser focal spot, only one emitter becomes excited (Figure 5) which will emit only one photon at a time, because of its finite fluorescence lifetime. To enhance the single-photon count rate (the bit rate of quantum communication system), and to provide directionality and polarization selectivity, a single emitter should be placed into a microcavity environment. The physics of spontaneous emission enhancement in microcavities is governed by the Purcell factor F_P [61,62] which is defined as $F_P = \gamma_c/\gamma_0$, where γ_c and γ_0 are the emitter decay rates with and without a cavity, respectively:

$$F_P = \frac{3Q(\lambda/n)^3}{4\pi^2 V_0}\left(\frac{|\boldsymbol{d}\cdot\boldsymbol{E}(r)|}{|d|\cdot|E(r)|}\right)^2, \qquad (1)$$

where Q is the cavity quality factor, λ the free-space wavelength of light, n the cavity refractive index, V_0 the cavity mode volume, d the emitter dipole moment, and $\boldsymbol{E}(r)$ the local electric field at the position r of the emitter. Equation (1) predicts enhancement or diminishing of F_P, depending on the ratio $Q\lambda^3/(V_0 n^3)$, and how the incident field is aligned with respect to the dipole moment, $\boldsymbol{d}$.

In Section 2 of this paper, experimental results of room temperature, robust SPSs with definite polarization using single-emitter fluorescence in either cholesteric (Section 2.1) or nematic (Section 2.2) LC hosts are discussed.[28–34,36–39] A desirable polarization state (either circular with definite handedness or linear with definite direction) of a fluorescence of the emitter in a LC host can be produced either by providing a chiral microcavity environment of a planar-aligned cholesteric liquid crystal (CLC) layer (Section 2.1) or by aligning emitters' dipole moments in a definite direction in a planar-aligned nematic LC (Section 2.2). Section 2.1 describes also antibunching and circularly polarized (CP) resonance with definite handedness in nanocrystal quantum dot (NQD) fluorescence in a glassy oligomeric cholesteric photonic bandgap microcavity. 4.9 times intensity enhancement was observed in such a microcavity in comparison with a polarization component with opposite handedness.[29]

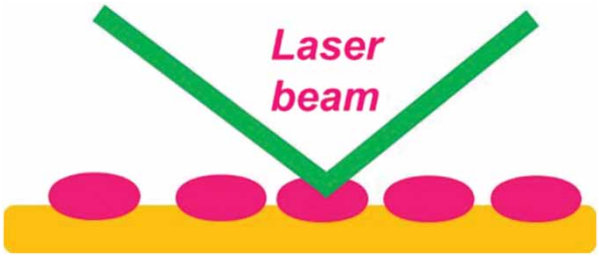

Figure 5. Principle of obtaining single (antibunched) photons.

It should be noted that room temperature SPSs based on single emitters in CLCs microcavities are much easier in fabrication, lower in cost, and more robust in comparison with well-developed cryogenic SPSs based on semiconductor heterostructured quantum dots fabricated by molecular beam epitaxy with microcavities prepared with high-precision electron beam lithography and focused ion beam etching.[47,48,51] Definite linear polarization of single photons from heterostructured quantum dots both in elliptical pillar microcavities and in an elliptical microcavities in 2-D photonic crystals were reported for resonance wavelength at *cryogenic* temperatures only, because only at cryogenic temperatures heterostructured quantum dots can emit single photons.[47,48,51] These cryogenic devices cannot be used in practical quantum communication systems.

Recently room temperature SPS operation was reported (including our own paper) using Bragg-reflector microcavities with single colloidal NQDs deposited in the defect layer between two Bragg reflectors.[32,39,50,63] The drawback of this structure is the existence of leaky (waveguide) modes along the surface of Bragg reflectors. To avoid these waveguide modes and to obtain definite linear polarization of emitted single photons, Bragg-reflectors should be etched by a focused ion beam to elliptical micropillar shapes which is difficult to implement. In difference with conventional Bragg reflectors with abrupt changes of refractive indices, refractive index of CLCs is changing monotonically, so that the leaky modes in 1-D-photonic bandgap CLC layers are very weak and no micropillar structure is needed to avoid losses. In addition, cholesteric microcavity chirality provides *definite circular* polarization of single photons. These chiral 1-D photonic-bandgap structures can enhance fluorescence of single emitter. Another important advantage of CLC photonic bandgap structures is the simplicity of their fabrication in comparison with vacuum-deposited Bragg reflectors as well as photonic bandgap structures prepared by electron beam and focused ion beam lithographies. Different types of single emitters can be easily dissolved or dispersed both in monomeric (fluid-like) or oligomeric (solid) LCs. Single-molecule dipoles can be aligned with LC molecular dipoles to produce single photons with *definite linear* polarization.

LC technology has another advantage. Special treatment of LCs (oxygen depletion) can protect the emitters from bleaching. Figure 6 shows our results on a significant diminishing of terrylene dye bleaching by saturation of monomeric LC with helium (oxygen depletion).[28] Another remarkable advantage of LCs is, for example, changing its properties with temperature or by

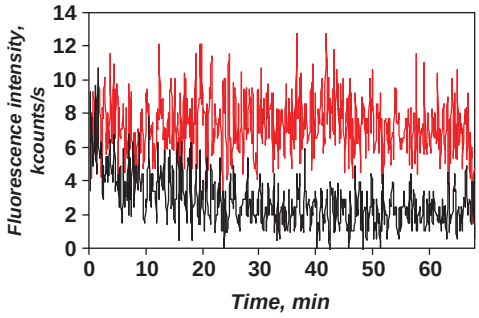

Figure 6. Fluorescence bleaching behavior of an assembly of terrylene dye molecules as a function of time for oxygen-depleted LC (red curve) and for LC without special oxygen depletion (black curve).

external-field variation can provide SPS tunability. As single emitters, we used NQDs, single nitrogen vacancy (NV)-color centers in nanodiamonds, and single dye molecules. We also started to work with nanocrystals doped with trivalent ions of rare-earths.

1.2. *Hong–Ou–Mandel interference with indistinguishable entangled photons: time interval measurements with femtosecond resolution*

In Section 3 of this paper, we report our results on simulating quantum mechanical barrier tunneling phenomena [40–42] using a planar-aligned nematic LC-filled double-prism structure. Quantum interference of two time-entangled photons in a Hong–Ou–Mandel interferometer [64] was used to measure with femtosecond (fs) resolution the single-photon tunneling time. The principle of a Hong–Ou–Mandel interference is explained in Figure 7 showing four possibilities of two photon propagation through a 50/50 beamsplitter in the case that each photon enters different input port of a beamsplitter. When two *identical* single photons enter different input ports of a 50/50 beamsplitter, photon "coalescence" takes place (Figure 7(b) and 7(c)) and no coincidence count between them will be recorded (a Hong–Ou–Mandel dip) if two detectors are placed at each of two output ports of a beamsplitter. If one photon is delayed with respect to the other, the probability of coincidence count detection will increase. So such an interferometer can measure the time intervals with high precision by measuring a shift of a Hong–Ou–Mandel dip.

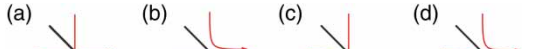

Figure 7. The four possibilities of two-photon reflection and transmission at a beam splitter.

Pairs of indistinguishable photons can be obtained in a spontaneous parametric down-conversion process (Figure 8, left).[65–69] For instance, using type I interaction [69] (Figure 8, right) in a single β-barium Borate (BBO) crystal, two time-entangled photons with the same polarization state and wavelength 2λ can be generated from an incident laser beam with a wavelength λ (Figure 8). In this case energy and momentum conservation should take place. This nonlinear optical process has a very low probability (conversion efficiency to one photon pair from a single-incident photon): approximately 10^{-10}–10^{-12} for a single mode with a 1 nm bandwidth, so to observe at least 1000 photon pairs/s, both high excitation intensities and single-photon counting detectors should be used.

In Section 3, Hong–Ou–Mandel interferometer with two indistinguishable entangled photons is described for high-precision measurements of the time delays in frustrated total internal reflection (FTIR).[41,42] It is commonly accepted that time delays in FTIR form an optical analogue to quantum mechanical tunneling times.[40, 70,71] Indeed, the evanescent waves supported by such a structure decay in a manner reminiscent of quantum mechanical wave functions in a potential barrier (Figure 9). Studying optical time delays in such structures can help us shed light on certain paradoxical tunneling phenomena. In Section 3, we present a nematic LC-filled double-prism structure that can be used to simulate a quantum mechanical barrier of variable height. The nematic LC's molecular director was tuned with an externally applied voltage to change the refractive index contrast, and consequently the critical angle of the glass–LC interface. At oblique incidence this is equivalent to tuning the effective barrier height.

It should be noted that the process of quantum mechanical barrier tunneling, whereby a particle of energy E

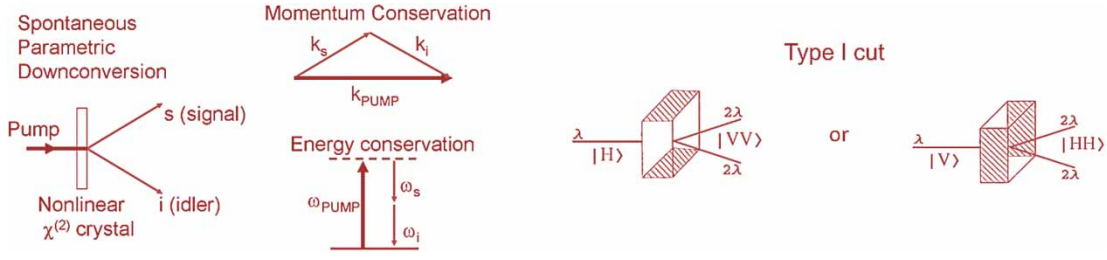

Figure 8. Spontaneous parametric down conversion: Left – schematics and conservation of energy and momentum. Right – type I interaction (signal and idler photons have the same linear polarizations).

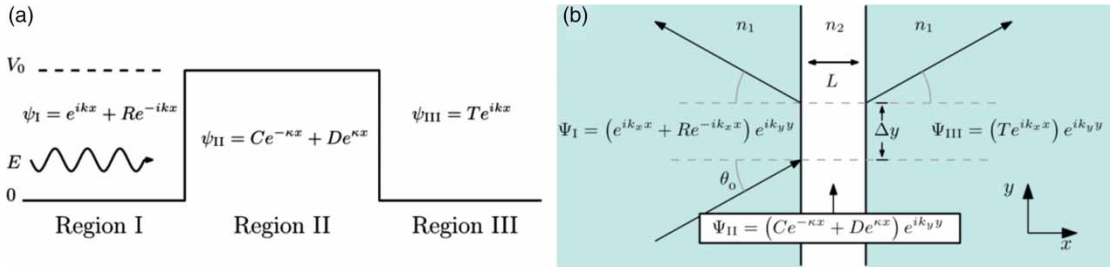

Figure 9. (a) Tunneling in quantum mechanics: a particle of energy E encounters a potential barrier of height V_0. (b) An optical analog to (a): a photon undergoes FTIR.

encounters a finite potential barrier of height $V_0 > E$, has been a topic of intense scrutiny for the better part of a century. Whereas the determination of the transmission and reflection probabilities is a fairly straightforward exercise in undergraduate quantum mechanics, the time delay experienced by the particle has been the cause of much controversy. The traditional definition of the group delay τ_g acquired when tunneling through a barrier of length L is calculated by the method of stationary phase, and is frequently called the phase time or Wigner time.[72] Surprisingly, the group delay can, under certain conditions, become shorter than the "equal time" c/L, suggesting superluminal transit of the tunneled particle. Many attempts have been made to resolve this apparent paradox,[73] and the ongoing debate has made it evident that further experimental investigations of these effects are required. In Section 3, using AC-voltage control of planar-aligned nematic LC layer in double-prism structure we showed experimentally that the contribution of the Goos–Hänchen shift (a small lateral shift as a coherence phenomenon of a linearly polarized finite beam when it reflected) to the tunneling delay is suppressed in FTIR.[40–42]

2. Polarized SPSs based on single-emitter fluorescence in LC hosts

The structure of this section is as follows. Section 2.1 describes photon antibunching and CP resonance with definite handedness in NQD fluorescence in a *glassy CLC oligomer* photonic bandgap microcavity as well as observed intensity enhancement in comparison with a polarization component with opposite handedness. The results on SPSs with definite circular polarization based on CLC *monomeric* structures doped with single NQDs are presented as well. Section 2.2. is devoted to linearly polarized fluorescence with a definite polarization state from single dye molecules aligned in both glassy oligomer and monomer nematic LCs. Section 2.3 of this part describes photon antibunching from NV-color center in nanodiamond in LC host and CP fluorescence of definite handedness from nanocrystals doped with trivalent ions of rare-earths dispersed in LC host. For SPS applications usually we used dopant concentration of ~1–10 nM.

2.1. *SPSs with circular polarization of definite handedness*

2.1.1. *Single-photon generation, detection, and characterization units*

Figure 10 shows general schematic of experimental set up for single-photon generation, detection, and characterization. Single-photon generation unit consists of a confocal fluorescence microscope with a high numerical aperture (N.A.) objective which focuses a pulsed or continuous wave (cw)-laser beam on a cover glass slip with a single emitter in a microcavity. The sample is placed on a microscope table located on a piezo-translation stage for a raster scan of the sample around a focused laser beam. Fluorescence light is collected by the same objective. A dichroic mirror reflects laser light and transmits fluorescence light. Interference filters with 6–9 orders of magnitude attenuation further reject an excitation laser light. Single-photon detection and characterization unit represents a Hanbury Brown and Twiss intensity interferometer (correlator) which consists of a nonpolarizing beamsplitter, two single-photon counting, thermoelectrically cooled avalanche photodiode modules (APDs), and start–stop electronics to measure time intervals between two consecutive photons in pairs to prove photon antibunching.

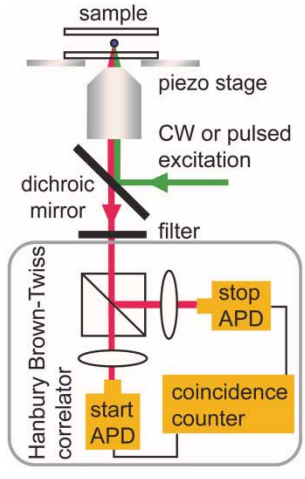

Figure 10. Schematic of a single-photon generation, detection, and characterization unit (APD – single-photon counting avalanche photodiode module). A Hanbury Brown and Twiss correlator is used for photon antibunching measurements.

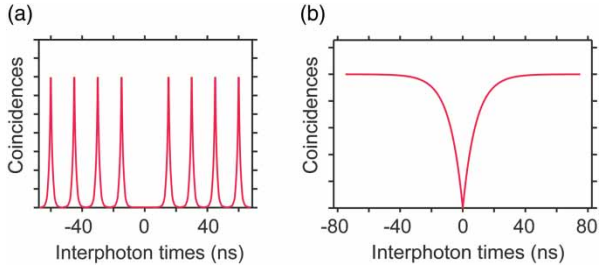

Figure 11. Photon antibunching histograms with dips at zero times for pulsed laser excitation (a) and for cw laser excitation (b). These histograms show how many second photons in consecutive photons pairs appear after first photons at definite time intervals (coincidences). The second-order correlation function $g^{(2)}(t)$ is proportional to coincidence count.

Figure 11 presents antibunching histograms with dips at zero time intervals for pulsed (a) and cw (b) excitations. These histograms show how many second photons (coincidences) in photon pairs appear at definite time interval after the first photons. To obtain a histogram with the second-order coherence function $g^{(2)}(t)$, a normalization is used: $g^{(2)}(t)$ is proportional to the number of coincidences. The characterization unit also contains electronics and software for confocal fluorescence imaging of single emitters. To increase confocal fluorescence imaging contrast, 150-μm detector areas serve as confocal microscope pinholes.

Figure 12 shows photographs of two experimental set ups used in our experiments. The left picture shows a home-built confocal fluorescence microscope based on a Nikon TE2000-U inverted microscope with several output ports for diagnostics. We excite our samples with several laser sources (76 MHz repetition rate, 6 ps pulse duration, 532-nm light from a Lynx mode-locked laser (Time-Bandwidth Products Inc.); 633-nm cw He-Ne laser; 976-nm diode laser; 514 nm cw argon ion laser). Two Si APDs SPCM AQR-14 (Perkin Elmer) were used as a single-photon counting detectors. The time intervals between two consecutively detected photons in separate arms of a Hanbury Brown and Twiss interferometer (covered by a black tissue) were measured by a TimeHarp 200 time correlated single-photon counting card with a start and stop inputs. A low light level, electron-multiplying, thermoelectrically cooled CCD-camera iXon DV 887 ECS-BV (Andor Technologies) was used both for spectral measurements with a Princeton Instruments (SpectraPro2150i) spectrometer and for a wide-field imaging of single-emitter fluorescence. Circular polarization measurements were accomplished using an achromatic quarter-wave plate and linear polarizer (LP). Our polarization data were calibrated for the effect of the optical system on CP light. We also performed a radiometric calibration of the optical system, including the spectrometer grating reflectivity dependence on polarization.

Figure 12, right, shows a WITec alpha-SNOM microscope with a Hanbury Brown and Twiss interferometer inside a metal box. For SPS applications, we used this microscope in a confocal transmission mode. A 532-nm, cw-laser was used for a single-emitter excitation.

2.1.2. *1-D photonic bandgap CLC structures*

Planar-aligned CLC structures exhibit a chiral 1-D photonic bandgaps for the handedness of CP light where the electric field vector follows the rotation of the CLC molecular director (Figure 13, left). The stop band is centered at wavelength $\lambda_o = p(n_e + n_o)/2$, where p is the pitch of the CLC spiral structure, and n_e and n_o are extraordinary and ordinary refractive indexes, respectively. The bandwidth of the transmission stop band is given by $\Delta\lambda \sim p(n_e - n_o)$.[74] Lasing in such CLC structures occurs at a band edge of this stop band.[9–17] In the similar way, to enhance single-emitter fluorescence in such a microcavity, single-emitter fluorescence maximum should correspond to a band edge of a CLC structure stop band.[29]

We prepared resonance planar-aligned cholesteric structures for single emitters with fluorescence in visible and near-IR (Figure 13, right) using both cholesteric oligomeric powders (Figure 13, right, top) and monomeric nematic fluids with chiral additives (Figure 13, right,

Figure 12. Two single-photon generation, detection, and characterization units used in experiments: Left – a home-made confocal fluorescence microscope with different diagnostics; Right – an alpha-SNOM WITec microscope comprising confocal, near-field, and an atomic force microscope with a Hanbury Brown and Twiss set up for antibunching measurements.

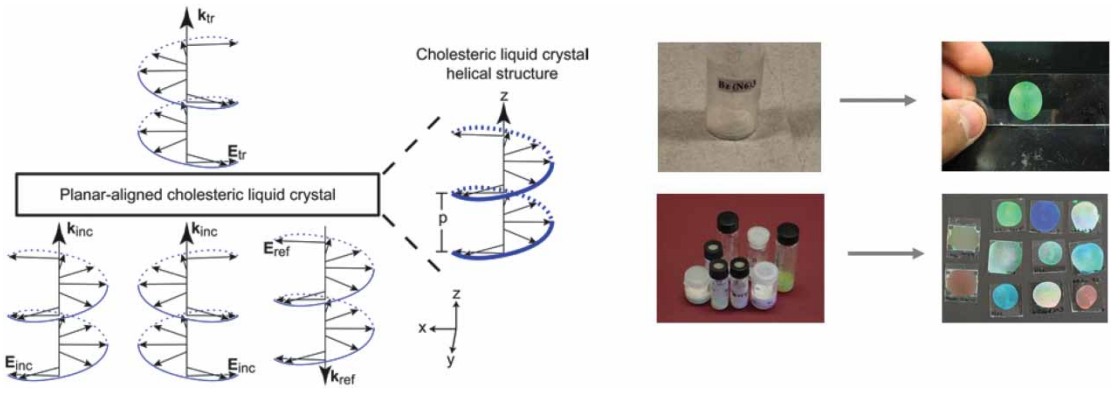

Figure 13. Left: Circular polarized light propagation in a 1-D photonic bandgap CLC structure. Right: Preparation of photonic bandgap CLC structures from a powder oligomer (top) and monomeric LCs (bottom).

bottom). One hundred and twenty micrometer-thickness cover-glass slips were employed as cell windows. For single-emitter excitation within a LC cell, a very tight focusing is important to excite only one emitter. For instance, with a 1-μm separation of single emitters, a diameter of an excitation laser focal spot should be of ~300–500 nm. To obtain such a small focal spot area, a high numerical aperture (N.A. = 1.35), oil immersion objective with a very short working distance (200 μm) was used in our experiments. In this case of very fragile substrates, a planar alignment using a buffing technique was challenging. We prepared a special mount in a buffing machine to fix these cover slips. For some experiments, we used photoalignment. In some cases, a decent planar alignment on a small area was obtained by a simple unidirectional motion of the cover slips relative to each other.

2.1.3. *SPS with a glassy oligomeric CLC microcavity doped with NQDs*

To prepare 1-D photonic bandgap CLC structure for this experiment, we used left-handed (LH) cyclosiloxane oligomeric CLC powder from Wacker Chemie [75] and produced a planar-aligned glassy CLC structure doped with CdSeTe NQDs, Qdot 800 ITK organic, Invitrogen, fluorescence maximum at 790 nm.[29] Doping was accomplished by heating the CLC to ~135 °C (the oligomer's melting temperature) and then mixing the melted CLC with quantum dots dispersed in toluene at a concentration of ~1 μM, with heating allowed to continue until the toluene evaporated. Subsequently, cells were prepared using two polyimide-buffed glass coverslips with thickness ~120 μm. The CLC doped with quantum dots was placed on a buffed coverslip and heated beyond the oligomer clearing temperature of 180 °C. After the sample was cooled to ~135 °C, the second buffed coverslip was placed on the first and sheared along the direction of polyimide buffing. A slow cooling process back to a glassy (solid) state preserved the CLC order. This resulted in a photonic bandgap microcavity with a center wavelength of 910 nm (Figure 14, blue curve).[29]

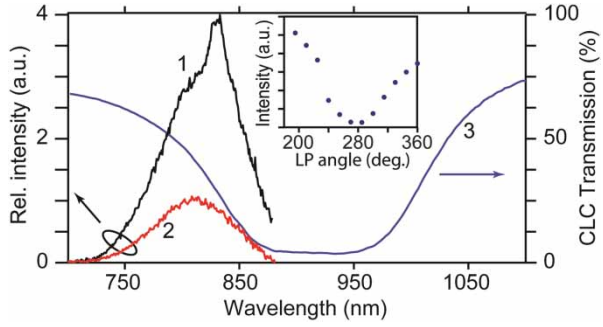

Figure 14. CP fluorescence resonance from NQDs doped in a glassy CLC microcavity. Curve 1: LHCP fluorescence spectrum of the NQDs with a resonance at 833 nm. Curve 2: RHCP fluorescence spectrum for the same NQDs. Curve 3: selective transmission of LHCP light through CLC microcavity. Inset: Dependence of resonance peak intensity on rotation of a LP after a fixed quarter wave plate. The measurements in insert were made when quantum dot bleaching is started, diminishing the maximum intensity ratio between LHCP and RHCP from a factor of 4.9 ($g_e = 1.3$) to a factor of 3.4 ($g_e = 1.1$). (Reproduced with permission [29]).

Prepared samples were analyzed using our home-made confocal microscope set up (Figure 12, left).[29] We excited the sample with cw, 633 nm laser light from a HeNe laser and observed the spectrum of the sample's fluorescence. By placing an achromatic quarter waveplate and LP in front of the spectrometer, we were able to filter for different handedness of CP fluorescence.

The resulting fluorescence spectra can be seen in Figure 14. LHCP light experienced the photonic bandgap and therefore the black LHCP curve in Figure 14 (curve 1) shows microcavity resonance, indicating that the LHCP light coupled to the cavity mode. The LHCP fluorescence had a center wavelength of 833 nm and a full width at half maximum (FWHM) of 16 nm ($Q \sim 50$), as compared to a FWHM of 76 nm for right-handed (RH) CP fluorescence. The center wavelength of this resonance roughly matches the edge of the photonic stop band, centered at 910 nm,

and shown in Figure 14 by the blue curve 3. The observed RHCP fluorescence is shown in red in Figure 14 (curve 2) and was less intense due to not experiencing the CLC microcavity, showing no sign of line narrowing. The maximum intensity ratio between LHCP and RHCP was a factor of 4.9. To characterize the degree of circular polarization, the circular polarization dissymmetry factor g_e is used:

$$g_e = \frac{2(I_L - I_R)}{(I_L + I_R)}, \tag{2}$$

where I_L and I_R are intensities of LHCP and RHCP light, respectively. At the wavelength of the resonance shown in Figure 14, $g_e = 1.3$. Note that for unpolarized light, $g_e = 0$, which we observed when NQDs were spin-coated on a bare glass slip.

Figure 15, left, shows a confocal fluorescence microscope raster scan taken of a sample prepared using a relatively low concentration of quantum dots dispersed in toluene (~10 nM), with the higher intensity spots indicating the location of fluorescing quantum dots in the glassy CLC microcavity. Focusing on a spot (circled in white on Figure 15, left), we checked for photon antibunching and obtained the coincidence histogram shown in Figure 15, right.

Figure 15, right, displays the histogram of coincidence counts $c(t)$ in blue, with $g^{(2)}(t)$ derived by normalizing $c(t)$. The measured $g^{(2)}(0)$ value from the fit shown in Figure 15 right (green, solid curve) is $g^{(2)}(0) = 0.382 \pm 0.037$. As $g^{(2)}(0) < 0.5$, this indicated that we have managed to isolate the fluorescence of a single quantum dot, serving as a source of antibunched light in a glassy CLC microcavity.[29]

2.1.4. *SPSs with monomeric CLC microcavities doped with NQDs*

Figure 16, left, shows a confocal microscope image of several single CdSe/ZnS NQD fluorescence in a monomeric 1-D photonic bandgap CLC structure (E7 and CB15). A 532-nm laser with 6 ps pulse duration and 76 MHz pulse repetition rate was used in this experiment. Figure 16, right (black and red solid curves) show emission spectra for

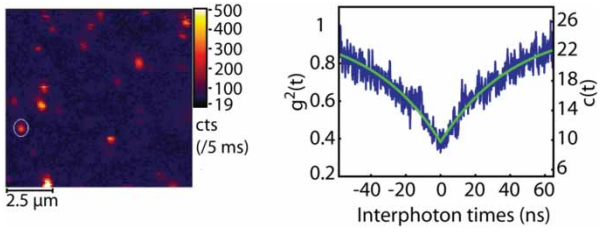

Figure 15. Left: Confocal fluorescence microscopy image of single CdSeTe NQDs in a glassy CLC photonic bandgap microcavity. Right: Raw coincidence counts $c(t)$ (right-hand scale) and $g^{(2)}(t)$ (left-hand scale), showing antibunching (dip at $t = 0$). (Reproduced with permission [29]).

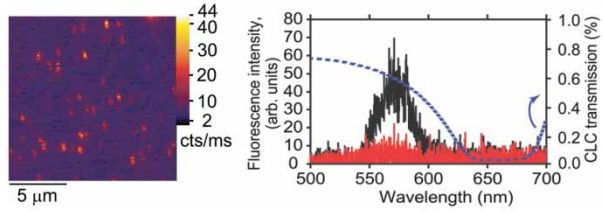

Figure 16. Left: Confocal fluorescence microscopy image of single CdSe NQDs in a monomeric CLC photonic bandgap microcavity. Right: Fluorescence spectrum of CdSe NQDs in the monomeric planar-aligned CLC host for two different circular polarizations of single photons (Black curve of high intensity – right handed – and red curve – left handed). CLC selective transmission curve is shown by a dashed blue line.

NQDs in a CLC microcavity for RH (black curve with high fluorescence intensity) and LH (red curve with low fluorescence intensity) circular polarizations.[32,33] Selective transmission curve of a CLC structure is shown as well (dashed blue curve). The degree of circular polarization measured by the dissymmetry factor g_e (Equation (2)) at 580 nm, is equal to −1.6, showing a RH circular polarization. For unpolarized light, $g_e = 0$. Using another type of CLC, for example, Wacker CLC oligomers, LH circular polarization of single photons can be obtained (see Section 2.1.3).

Figure 17, top left, presents the $g^{(2)}(t)$ histogram at different interphoton times t. One sees that the peak at zero interphoton time is clearly smaller than any of the other peaks, which shows an antibunching property [$g^{(2)}(0) = 0.76 \pm 0.04$]. Figure 17, top right, shows Raman spectrum

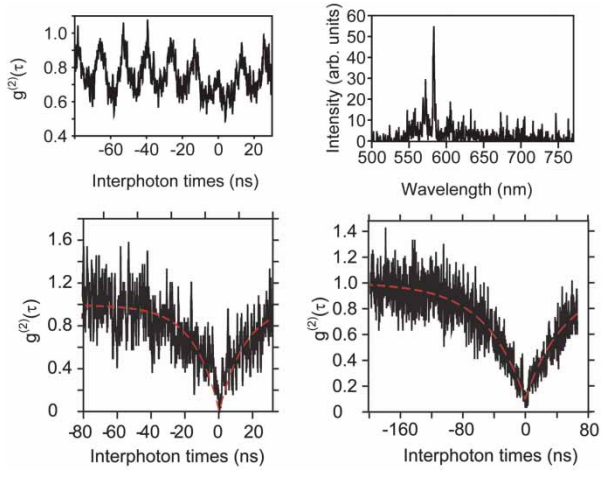

Figure 17. Top left: Histogram of coincidence counts of single CdSe NQD fluorescence ($\lambda_0 = 580$ nm) in a monomeric CLC host (E7 and CB 15 mixture) under pulsed excitation. The dip at zero interphoton time indicates antibunching. Top right: Raman spectra of E7 and CB 15 mixture without NQDs showing maximum at a fluorescence wavelength ~580 nm of a CdSe NQD. Bottom left and right: Antibunched fluorescence of CdSeTe NQDs ($\lambda_0 = 700$ nm) in a monomeric CLC host (E7 and CB 15 mixture) using 532-nm, pulsed (see explanation in the text) and 532-nm, cw excitation.

of undoped CLC. The peak near 580 nm is not a microcavity effect, because we observed the same features from unaligned CLC without a microcavity. This Raman spectrum of CLC explains relative high value of $g^{(2)}(0)$ in these experiments, but this antibunching histogram can be improved by using NQDs which fluorescence spectrum is outside the Raman spectrum of the CLC.

In order to avoid the CLC host Raman scattering, we selected CdSeTe NQDs with $\lambda_o = 700$ nm and doped them into the E7 and CB15 CLC host with the stop band edge at this wavelength. When illuminating a single NQD, we obtained antibunching with $g^{(2)}(0) = 0.001 \pm 0.03$ (Figure 17, bottom left). The spontaneous decay rate for these NQDs (20 MHz) is less than the laser excitation rate (76 MHz), so we cannot observe fluorescence excited by separate laser pulses as in Figure 17, top left.

Figure 17, bottom right shows the antibunching histogram for fluorescence of CdSeTe NQD with $\lambda_o = 700$ nm doped in the same E7 and CB15 CLC host illuminated with *cw*, 532 nm light in difference with a *pulsed*, 532-nm excitation in the case of Figure 17, bottom-left histogram. We observed antibunched fluorescence with $g^{(2)}(0) = 0.11 \pm 0.06$, also showing that only single photons are emitted.

These results show that using LCs as the host, to obtain better fluorescence antibunching of single emitters we should select emitters with fluorescence wavelength outside the host background, or use upconversion excitation process to excite single emitters.

2.1.5. *Cholesteric photonic bandgap microcavities doped with PbSe NQDs for SPSs at fiber-optical communication wavelengths*

One of the most difficult tasks in SPS implementation is to make a source of single photons for fiber optical communication networks with the low attenuation losses and zero dispersion around 1.3 μm, and with the most widely used 1.5 μm wavelength with the lowest attenuation losses and the longest range of propagation. University of Rochester, Chemistry Department (group of T. Krauss) developed PbS and PbSe NQDs with fluorescence at 1.3 and 1.5 μm. Figure 18 [32,33] shows our results on spectral transmission curves for several prepared cholesteric photonic bandgap structures with the band edge at 1.5 μm made of monomeric (E7 and CB15) CLC (left) and glassy Wacker oligomeric CLC (right). The fluorescence spectrum of a PbSe NQD solution at high NQD concentration with the maximum at 1.5 μm is depicted in both figures.

For the development of CLC hosts which form a chiral photonic bandgap tuned to the NQD fluorescence band, two main aspects are important: (1) properly choosing the concentration (or ratio) of different LC components and (2) providing planar alignment of the CLC. For the monomeric mixtures, the stop band position λ_c of the photonic bandgap is defined roughly by $C = n_{av}/(\lambda_c \times \text{HTP})$, where C is weight concentration of CB15 in the CB15/E7 mixture, $n_{av} \sim 1.6$ for this mixture, and HTP ~7.3 μm^{-1} is the helical twisting power of the chiral additive in nematic LC. The actual stop band position relative to the fluorescence maximum of the NQD was further defined empirically by obtaining selective transmission curves of different samples using a spectrophotometer. After monomeric CLC preparation, a NQD solution of ~1 nM concentration was mixed with monomeric CLC and solvent was evaporated.

For the oligomeric CLC powders there is not such a simple relation between the concentration and λ_c. We found the right ratio R of components only empirically by mixing the different ratios of two oligomeric CLC powders with different λ_c (1.17 and 2.15 μm) by dissolving them in a solvent. By evaporating the solvent using a procedure of heating this solution in a vacuum inside a rotating retort, we obtained a new powder oligomer with an intermediate λ_c.

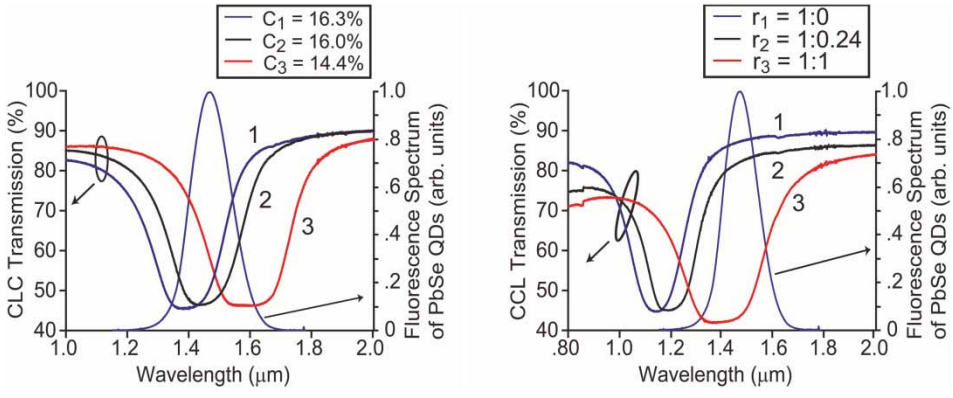

Figure 18. CLC photonic bandgap selective transmission curves in unpolarized light for NQDs with fluorescence at optical communication wavelength (1.5 μm) for either *monomeric* (left) or *oligomeric* (right) CLC. Also shown are PbSe NQD fluorescence spectra at 1.5 μm that these transmission curves were turned to. Left: The weight concentrations of chiral additive CB15 in CB15/E7 mixture are $c_m = 16.3\%$ (curve 1), 16.0% (curve 2), and 14.4% (curve 3). Right: The ratios of Wacker oligomeric powders with $\lambda_0 = 1.17$ μm and $\lambda_0 = 2.15$ μm are, $r_0 = 1:0$ (curve 1), 1:0.24 (curve 2), and 1:1 (curve 3).

After that, monomeric CLC doped with NQDs was placed between two cover glass slips with a standard planar alignment procedure. For planar alignment of oligomeric CLC, a cover glass slip with Wacker powder was placed on a hot plate and melted at ~120 °C. After a planar alignment with the second cover glass slip, the sample was slowly cooled into the glassy state preserving CLC order and planar alignment. For single-molecule fluorescence experiments Wacker powders need to be purified. In many cases, we purified CB15 and E7 as well using 0.3–5 μm particle filters.

2.2. *SPSs with definite linear polarization based on nematic LCs doped with single dye molecules*

Another intriguing application of LCs as hosts for single emitters is using the planar alignment of nematic LCs to provide doped molecular dipoles definite alignment along a preferred direction for efficient excitation. This allows for the creation of a SPS with fluorescence of definite linear polarization. For these experiments, we also used both glassy nematic oligomers and monomers.

2.2.1. *Linear polarization of single photons from a dye-doped glassy nematic oligomer*

A glassy nematic LC oligomer synthesized by S.H. Chen's group of University of Rochester was doped with $DiIC_{18}(3)$ dye (DiI) molecules from Molecular Probes.[31, 34] Planar-aligned layers of this doped LC host of ~100 nm thickness were prepared using photoalignment of the LC molecules. Photoalignment was performed by spin-coating a Staralign-2100 linearly photopolymerizable polymer (Rolic Technologies Ltd.) to a cleaned cover glass slip, which was then cured at ~135 °C. This film was then irradiated by a polarized UV light for 10–15 min, with further irradiation used to bleach the polymer impurity fluorescence.[31,34]

An oligomer solution doped with dye and diluted in chloroform was subsequently spin-coated onto these Staralign-coated glass slips. After the chloroform evaporated, we heated the sample to ~80 °C, slightly above where the oligomer transition to a nematic state occurs, after which the sample was slowly cooled to a glassy state, preserving the planar-aligned nematic order.

To characterize prepared samples, we used the WITec alpha-SNOM (Figure 12, right) in a confocal mode, exciting the sample using a cw, 532-nm Nd:YAG laser excitation. A schematic diagram of the experimental set up is shown in Figure 19. Single-photon counting avalanche photodiodes were used as photodetectors for confocal fluorescence scans, with a polarizing beamsplitter used so that each photodetector collected light of orthogonal polarizations.

DiI dye molecules doped in a planar-aligned LC host tend to fluoresce with polarization *perpendicular* to the

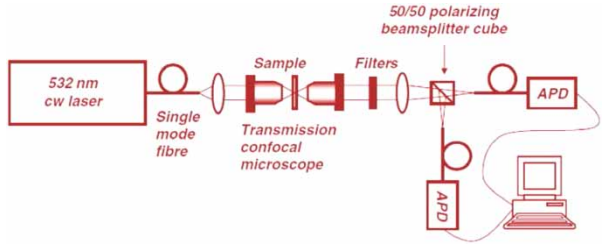

Figure 19. Experimental set up for polarization measurements using a modified WITec microscope (Figure 12, right).

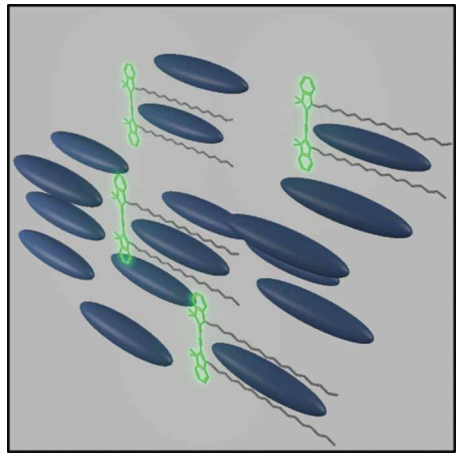

Figure 20. Schematic view of DiI dye molecules in a nematic LC host. The long axis (alkyl chains) of the DiI molecules tend to orient themselves along the rod-like nematic molecules, while the dipole, which is parallel to the bridge between the alkyl chains, orients perpendicular to the direction of LC alignment.

alignment of the LC. It can be explained by the molecular structure of these molecules. As illustrated in Figure 20, it is likely that two alkyl chains of these molecules orient themselves parallel to the rod-like molecules of the nematic LC host. The absorbing and emitting dipoles, however, are parallel to the bridge between these alkyl chains. Therefore, these dipoles end up oriented perpendicular to the direction of LC alignment, hence the fluorescence having a polarization orthogonal to the alignment of the LC. Figure 21 shows confocal microscope raster scan images of DiI single-molecule fluorescence for polarization components perpendicular (left) and parallel (right) to nematic alignment direction.

Thirty-eight single molecules were identified by the peak pixel intensity values (with background subtraction) and a linear polarization measure ρ was determined for each molecule by comparison of the "perpendicular" and "parallel" polarization images. In the experiments on single-emitter fluorescence microscopy a very sensitive single-photon counting detector modules are used. With such sensitivity photon counts appear from almost every material under laser excitation, including glass or quartz substrates, interference filters, and oil immersion liquids as well as LC materials and polymer layers. Incident laser

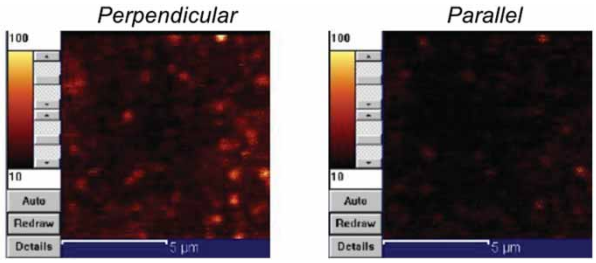

Figure 21. Confocal fluorescence microscopy images of DiI dye single-molecule fluorescence in a planar-aligned, glassy, nematic LC host ($10 \times 10\,\mu$m raster scan). Left: Polarization perpendicular to the alignment direction; right: parallel polarization. Scale shows counts/pixel.

light can also contribute to a background in spite of 9–12 orders of magnitude attenuation. This background is low in our experiments (less than 10 kcount/s for 100–200 kcounts/s of the signal) and uniform across the sample area. Our measure of linear polarization was

$$\rho = \frac{(I_{\text{par}} - I_{\text{perp}})}{(I_{\text{par}} + I_{\text{perp}})}, \tag{3}$$

where I_{par} and I_{perp} are, respectively, the fluorescence intensities parallel and perpendicular to the direction of alignment. The only difference of ρ with the degree of polarization is that it allows inclusion of the *direction* of polarization as part of the measure, depending on whether ρ is positive or negative.

The different ρ values that we found are histogrammed in Figure 22, left. A clear asymmetry in Figure 22, left demonstrates a preference toward fluorescence polarized perpendicular to sample alignment. This is in contrast to the expected fluorescence from an unoriented sample, which would yield a symmetric ρ histogram relative to $\rho = 0$.

To confirm these results, additional experiments were carried out. Figure 22, right, shows spectrofluorimeter measurements made for polarization perpendicular and parallel to the sample alignment, this time having used a sample of planar-aligned glassy nematic LC oligomer doped with DiI molecules of more than 1% concentration by weight. The value of ρ was measured by comparing the peak intensities of the curves, yielding $\rho = -0.5$. The results of Figure 22 indicate a clear preference for fluorescence with definite linear polarization perpendicular to the sample alignment in the case of DiI dye molecules doped in a planar-aligned nematic LC host.

2.2.2. *Linear polarization of single photons from a dye-doped nematic monomer mixture E7*

These experiments were carried out on a set up presented in Figure 12, left.

Figure 23, left, shows intensity changes of fluorescence of DiI molecules in a planar-aligned monomeric nematic LC (E7), as the linear polarization of the excitation 532-nm

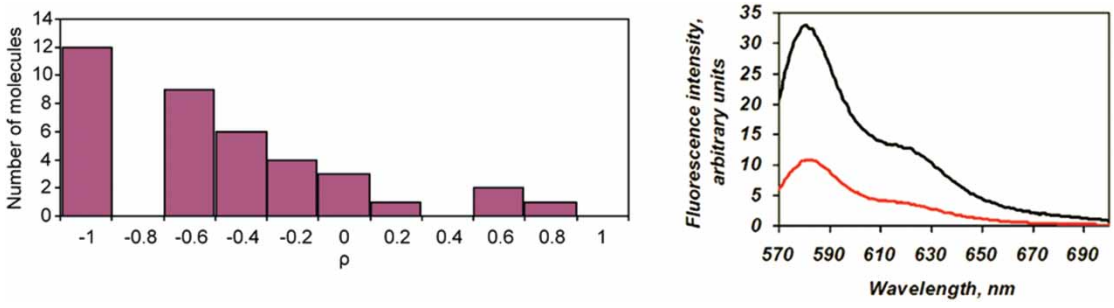

Figure 22. Left: Asymmetric histogram of polarization measure ρ from 38 different DiI dye molecules in a planar-aligned glassy nematic LC host showing linear polarization distribution of single dye molecules. For random polarization a histogram will be symmetrical. Right: Polarized fluorescence of DiI dye molecules in planar-aligned glassy nematic LC at *high concentration* of dye molecules. Black and red curves show fluorescence spectrum with polarization perpendicular and parallel to the host alignment direction.

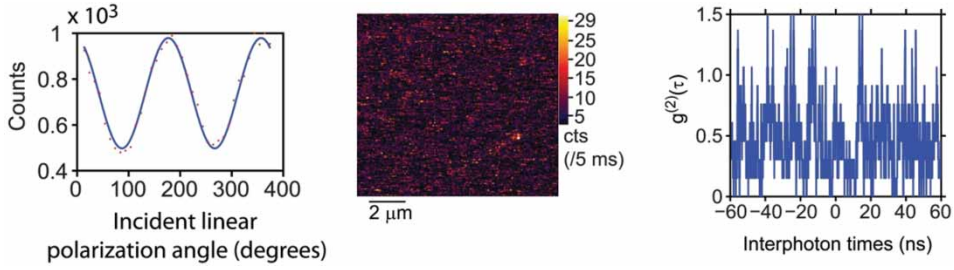

Figure 23. Left: Intensity of DiI fluorescence in planar-aligned E7 nematic LC as linear polarization of excitation laser light was rotated over 360°, with red dots showing experimental measurements and the blue solid curve providing a sinusoidal fit. The zero angle of polarization corresponds to the direction perpendicular to LC alignment. Center: A confocal microscope image of single DiI molecule fluorescence in a planar-aligned E7 nematic LC host. Right: Antibunching histogram of DiI molecule fluorescence in a planar-aligned E7 nematic LC host showing a dip at zero interphoton time.

laser beam was rotated over 360°. This figure shows a clear dependence of the fluorescence intensity on the exciting angle of polarization, where the maximum fluorescence occurred when the DiI molecules were excited by light with linear polarization perpendicular to the alignment of the LC.[39]

Figure 23, center and right, shows a confocal fluorescence microscope image and an antibunching histogram for a single molecule of DiI dye doped in an E7 nematic host, taken using pulsed, 532 nm excitation, respectively. The value for $g^{(2)}(0)$ is $g^{(2)}(0) = 0.77 \pm 0.10$.[39] This relatively high value of $g^{(2)}(0)$ may be due to the fact that the Raman spectrum of the E7 overlaps with the fluorescence spectrum of DiI dye.

2.3. *Rare-earth-doped nanocrystals and color centers in nanodiamonds in LC hosts*

Additional work with monomeric CLC-based microcavities included doping with emitters such as nanocrystals with trivalent rare-earth ions and nanodiamonds with NV color centers. These alternative emitters can provide a source of single photons without emitter bleaching. We also started to work with other unbleachable single emitters – nanodiamonds with Si-vacancy color centers (which have 10 times narrower fluorescence spectral line than a NV color center), and with single-walled carbon nanotubes (which can be aligned by LC molecules).

2.3.1. *Cholesteric photonic bandgap microcavity with rare-earth-doped nanocrystals*

A monomeric CLC microcavity made from a mixture of E7 and CB 15 was doped with rare-earth Er^{3+} and Yb^{3+} ions in 20–30 nm-sized $NaYF_4$ nanocrystals with 20% Yb and 2% Er. When these ions were excited using a cw, 976 nm diode laser at incident powers of ~500 μW, we were able to observe upconverted fluorescence of Er^{3+} in visible, as shown in Figure 24, left (red solid curve). The blue dashed curve shows the spectral transmission of CLC microcavity measured with unpolarized light.

Energy levels of Er^{3+} and Yb^{3+} and upconversion excitation scheme under 980 nm excitation are shown in Figure 24, right. The emission lines observed were attributed to the transitions $^2H_{11/2}$, $^4S_{3/2} \rightarrow {}^4I_{15/2}$ (green) and $^4F_{9/2} \rightarrow {}^4I_{15/2}$ (red) of the Er^{3+} ions. The populations of upper levels in Er^{3+} occur due to an efficient energy transfer from the Yb^{3+} to the Er^{3+}. This fluorescence was measured to have a circular polarization dissymmetry factor of $g_e = -0.77$ at 680 nm.[39] These nanocrystals doped with rare-earth ions were prepared at the University at Buffalo (The Institute for Lasers, Photonics, and Biophotonics). It should be noted that Er^{3+} ions also have a fluorescence line at ~1.5 μm, which is important for fiber-optical communication.

2.3.2. *Single photons from NV-center nanodiamonds in a CLC host*

Figure 25, left, shows a photon antibunching histogram from NV color center in nanodiamond in a CLC (E7 and CB15) microcavity with a stop band centered at 725 nm, under cw, 514 nm argon ion laser excitation. The $g^{(2)}(0)$ value determined via fit (shown in Figure 25, left, as the dashed red line) was $g^{(2)}(0) = 0.74 \pm 0.08$.[39] The fluorescence spectrum of NV centers in nanodiamonds doped in this monomeric CLC when excited using cw, 514 nm excitation is presented in Figure 25, right. These nanodiamonds were purchased from Microdiamant AG, Switzerland. They are agglomerate free and ~30–50 nm in diameter.

3. Simulating quantum mechanical barrier tunneling phenomena with a nematic LC-filled double-prism structure

3.1. *Theory of measuring tunneling times: Fabry-Pérot resonances and tunneling regime*

The measurements of tunneling times in 1D-quantum mechanical systems lies at the heart of the understanding

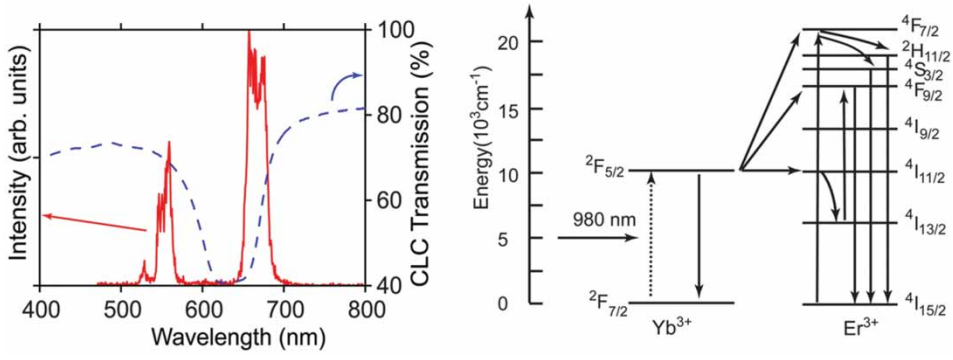

Figure 24. Left: Red solid lines: Fluorescence spectrum of Er^{3+} ions doped in $NaYF_4$ nanocrystals dispersed in a chiral CLC microcavity (E7 and CB15). The blue dashed curve shows the spectral transmission of CLC microcavity measured with unpolarized light. Right: Energy levels of Er^{3+} and Yb^{3+} and upconversion excitation scheme under 980 nm excitation.

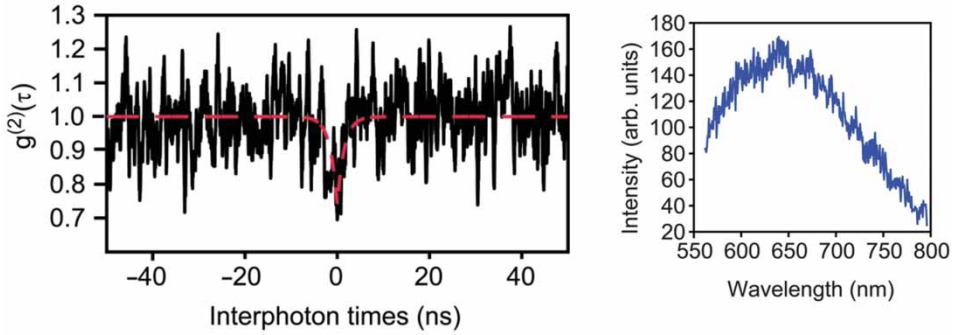

Figure 25. Left: Photon antibunching from NV center nanodiamond in a monomeric CLC host. Black curve shows the raw data. Red dashed curve shows the fit. Right: Fluorescence spectrum of NV centers in nanodiamonds in a monomeric CLC host (cw, 514-nm laser excitation).

of many quantum mechanical phenomena. It is commonly accepted that time delays in FTIR represent an optical analog to these quantum mechanical tunneling times due to the formal similarity of the Helmholtz and Schrödinger equations. A number of authors have addressed this analogy over the last 25 years, focusing primary on glass–air–glass double-prism structures. Foremost among the discussion are the questions of what exactly causes the time delay one would observe experimentally in such a system. One would expect that the Goos–Hänchen shift [76,77] would make a sizable contribution to the measured time delay. The Goos–Hänchen shift Δy (see Figures 9(b) and 26, left) is a phenomenon of classical optics in which a finite light beam reflecting off a surface is spatially shifted on the distance of the order of a wavelength as if it had briefly penetrated the surface before reflecting back. In this section, we present experimental evidence that the contribution of the Goos–Hänchen shift to the tunneling delay is in fact negligible in this two-dimensional tunneling system.

Consider the double interface system shown schematically in Figure 9(b). Light incident at an angle θ from a region of high refractive index n_1 encounters an interface with a material of lower index n_2. If the light is incident above the critical angle, the Helmholtz equation admits the following stationary-state solutions: in region I, the incident and reflected plane waves Ψ_i and Ψ_r, respectively, in region III the transmitted wave Ψ_t, and in the barrier region the exponentially decaying solutions $\Psi^{(+)}$ and $\Psi^{(-)}$. Analytically, we can write:

$$\begin{aligned}\Psi_{\mathrm{I}} &= \Psi_{\mathrm{i}} + \Psi_{\mathrm{r}} = (e^{ik_x x} + R\,e^{-ik_x x})\,e^{ik_y y},\\ \Psi_{\mathrm{II}} &= \Psi^{(-)} + \Psi^{(+)} = (C\,e^{-\kappa x} + D\,e^{\kappa x})\,e^{ik_y y},\\ \Psi_{\mathrm{III}} &= \Psi_{\mathrm{t}} = (T\,e^{ik_x x})\,e^{ik_y y},\end{aligned} \tag{4}$$

where the coefficients R, C, D, and T are deduced from the boundary conditions. An analogy can be made between the height of the barrier V_0 for the particle with energy E in Figure 9(a) and the index contrast n_2/n_1 in Figure 9(b):

$$\frac{E}{V_0} \leftrightarrow \frac{\cos^2\theta}{1-(n_2/n_1)^2}. \tag{5}$$

This analogy allows us to explore the intricacies of the quantum mechanical barrier tunneling phenomenon by measuring the optical time delay in FTIR as a function of the index of the barrier region.

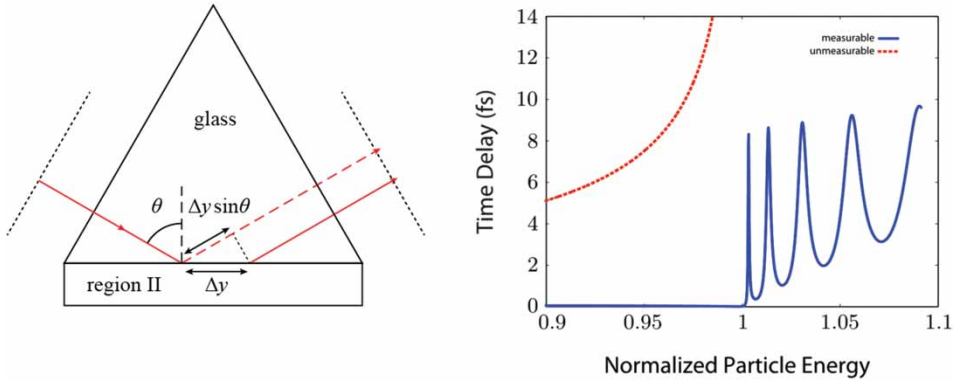

Figure 26. Left: Total internal reflection at the interface between an equilateral prism and a dielectric slab. The Goos–Hänchen shift Δy causes a change in the glass propagation length, which has ramifications for an experimental measurement of tunneling delay in the double-prism geometry. Right: *Measurable* and *unmeasurable* parts of the total tunneling group delay plotted against the normalized particle energy $\cos^2\theta_0/(1-(n_2/n_1)^2)$ for a photon undergoing FTIR for different values of n_2. In this simulation, $L = 8\,\mu\mathrm{m}$, $\theta_0 = 63.5^\circ$, $\lambda = 727\,\mathrm{nm}$, and $n_1 = 1.77$. (Reproduced with permission [40]).

There are several possible definitions of tunneling delay, and a thorough review would be outside the scope of this paper. We will, therefore, concentrate on the one most directly applicable to optical experiments. Most optical direct-time delay measurements are sensitive to the group delay τ_g, which represents the time-of-arrival of the peak of a Gaussian pulse/wavefunction in the absence of severe distortion. This can be calculated in a straightforward manner once the transmission coefficient T is known:

$$\tau_g = \left(\frac{\partial\phi_0}{\partial\omega}\right)_{\theta_0} - \frac{\tan\theta_0}{\omega}\left(\frac{\partial\phi_0}{\partial\theta_0}\right)_{\omega}, \quad \phi_0 = \arg T + k_x L. \tag{6}$$

The first term in this expression, $\partial\phi_0/\partial\omega$, describes the delay contribution from the tunneling along the X-direction, while the second term gives the contribution to the total group delay that is due to the Goos–Hänchen shift Δy. L is the length of the medium with lower refractive index n_2. As it was explained in our theoretical paper,[40] the Goos–Hänchen contribution is suppressed in experimental implementations of FTIR. Any delay incurred through the k_y component is identically compensated by a reduction in glass propagation length (Figure 26, left). We shall, therefore, refer to these two terms in Equation (6) as the *measurable* and *unmeasurable* portions of the total group delay.[40]

These quantities are plotted as a function of the normalized particle energy $\cos^2\theta_0/(1-(n_2/n_1)^2)$ in Figure 26, right. Two distinct regimes are observed:

(1) When $\cos^2\theta_0 > 1-(n_2/n_1)^2$, propagation in the barrier region is allowed and Fabry-Pérot resonances are observed.
(2) In the tunneling regime, when $\cos^2\theta_0 < 1-(n_2/n_1)^2$, the Goos–Hänchen contribution dominates the total photonic delay and is orders of magnitude larger than the measurable portion.

To observe this behavior experimentally, we have developed a liquid-crystal-filled double-prism structure where the index contrast can be tuned electronically.

3.2. *Description of the double-prism structure with a nematic LC layer*

The double-prism structure considered here is shown schematically in Figure 27. A planar-aligned nematic LC cell with transparent indium–tin–oxide (ITO)-coated glass substrates is sandwiched between two equilateral glass prisms. To observe FTIR, a large index contrast between the LC layer and the substrates is required. For that reason, both the cell substrates and the prisms are made of high-index N-SF11 glass, which at $\lambda = 727$ nm has a refractive index of $n = 1.77$. A small amount of index-matching

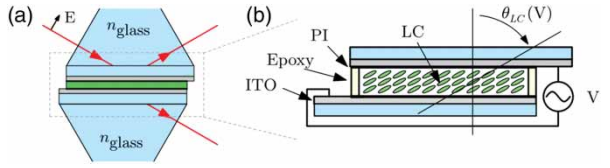

Figure 27. Diagram of the double-prism structure. In (a) a LC cell is sandwiched between two equilateral glass prisms. An exploded diagram of the LC cell is shown in (b). The substrates are coated with transparent ITO electrodes to facilitate electronic control of the LC molecular director rotation angle θ_{LC}, and thin PI to aid the alignment of the LC layer. (Reproduced with permission [41]).

fluid ($n = 1.70$) is applied to the prism-cell interfaces to minimize unwanted reflections.[41,42]

The LC cell preparation proceeds as follows:

(1) Two 3-mm thick N-SF11 substrates are sputter coated with 30-nm layers of ITO to serve as electrodes.
(2) Next, an approximately 15-nm alignment layer of polyimide is spin-coated on top of the ITO. The substrates are then subjected to a unidirectional mechanical buffing technique that shears the polyimide layer (PI), causing the LC molecular director to preferentially align along the buffing direction when the cell is filled.[78] The cell is then constructed by placing spacers between the two processed faces: small amounts of 5-min epoxy mixed with 5-μm glass beads are placed on the four corners of the cell, and pressure is applied while the epoxy mixture cures. The void thickness of cells prepared with this technique is typically in the range of 8–12 μm.
(3) The cell is then filled with a uniaxial nematic LC mixture (E7: Merck) through capillary action. The edges of the cell are sealed with epoxy after filling to prevent evaporative loss and deterioration of the LC.
(4) Finally, wires are attached to the exposed ITO sections with conductive silver epoxy to allow for electronic control of the LC molecular director.

3.3. *Simulation of device performance under realistic conditions. Nematic molecular director rotation under AC-voltage*

To accurately simulate the performance of this device under realistic laboratory conditions, the rather simplistic model of Section 3.1 must be extended to account for the anisotropy and disorder of the LC layer, and allow for a spread of input k-vectors. This can be accomplished by numerically solving Maxwell's equations in 4×4 matrix form for a multilayer slab structure.[79] Using this technique, the complex reflection and transmission coefficients

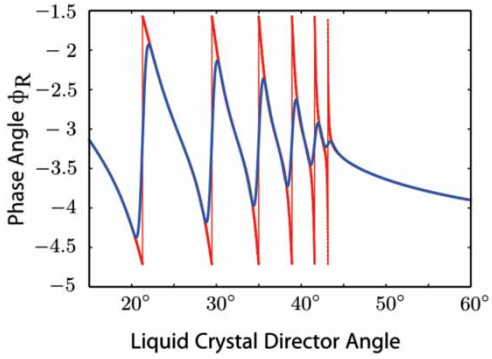

Figure 28. The predicted phase of the reflection coefficient based on the 4×4 matrix method described in the text for 727-nm light incident on an 8-μm LC cell. The parameters used are $\theta = 63.5°$, $n_{\text{glass}} = 1.77$, $n_{\text{e}} = 1.63$, and $n_{\text{o}} = 1.54$. The resulting phase is then convolved with a Gaussian function to account for a spread of input k-vectors (blue solid line).

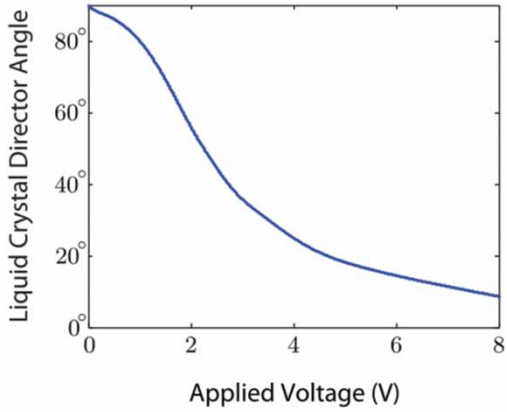

Figure 29. Dependence of the LC molecular director angle on applied voltage obtained from transmission measurements. We did not measure a pretilt angle, so 90° in the plot is an approximate value.

are calculated as functions of the photon's frequency, its incidence angle, and the LC molecular director angle.

Figure 28 shows the calculated phase ϕ_R of the reflection coefficient as a function of the LC molecular director angle. In this simulation, the light is incident at $\theta_0 = 69.3°$ from a glass region of refractive index $n_{\text{glass}} = 1.77$ onto an 8-μm-thick LC cell. The extraordinary and ordinary refractive indices used for the LC are $n_e = 1.63$ and $n_o = 1.54$. These indices are a little lower and higher, respectively, than the expected values for E7 to correct for LC disorder. Since this method assumes plane wave incidence, we have convolved the phase with a Gaussian function to account for the spread of incidence angles present in our experiment (Figure 28, blue solid line).

The expected optical time delay in reflection from this structure, $\partial\phi_R/\partial\omega$, can be calculated as a function of applied AC-voltage once the voltage dependence of the LC molecular director angle is known. This can be empirically determined from single-wavelength transmission measurements.[80] The LC cell is placed between a polarizer and an analyzer and illuminated by a HeNe laser ($\lambda = 632.8$ nm) at normal incidence such that the input polarization is at 45° to the buffing direction. Transmission measurements are then taken as a function of applied AC-voltage for both crossed and parallel analyzer configurations. The LC molecular director rotation angle can then be deduced from the ratio of the transmitted intensities.

The resulting behavior is shown in Figure 29. In the absence of a driving AC field, the buffing process performed on the polyimide alignment layer causes the LC molecules to orient themselves along the direction of buffing, perpendicular to the surface normal ($\theta_{\text{LC}} \sim 90°$). In practice, there is some pretilt angle which we did not measure since it was not critical to our Hong–Ou–Mandel experiments. When an AC-voltage is applied across the electrodes, it supplies a torque that twists the LC molecular director toward the surface normal.

3.4. *Measuring time delays with fs precision using a Hong–Ou–Mandel interferometer with entangled photons*

Optical time delays in reflection from a double-prism structure with an electrically controlled nematic layer were measured with fs precision using a Hong–Ou–Mandel interferometer.[64,81] In our experimental set up (Figure 30, left) [41,42], time-entangled photon pairs of linearly polarized photons are generated through type I spontaneous parametric downconversion in a 3-mm thick BBO crystal that is pumped by a 1-W cw-argon-ion laser ($\lambda = 363.8$ nm). Interference filters set the photon's bandwidth to be 10 nm, centered around 727.6 nm. One photon is sent through a path of known length while the other is sent to a test arm that contains the double-prism structure. The photons are then recombined in a 50–50 beam splitter whose output ports are monitored in coincidence through single-mode optical fibers by APD single-photon counting modules (Perkin-Elmer SPCM-AQR-14-FC) with low dark count (less than 100 counts/s) and a quantum efficiency of approximately 70% at 727 nm. The length of the known arm is varied using a 50-μm-range of stage movement in 1-μm increments. At each stage position we record the LC voltage, integration time, singles count on each detector, and coincidence counts. When the interferometer is balanced, both photons exit from the same port and the coincidence count rate is reduced. The position of complete destructive interference can be determined with sub-fs resolution, though in practice the resolution may be limited by thermal drifts or other sources of noise. This procedure is repeated for different applied AC-voltages on a nematic cell, and the shift of the Hong–Ou–Mandel dip relative to $V = 0$ is used to extract the time delay.

The experimentally measured reflection time delays with a typical Hong–Ou–Mandel dip from our measurements are shown in Figure 30(b), along with a plot of the

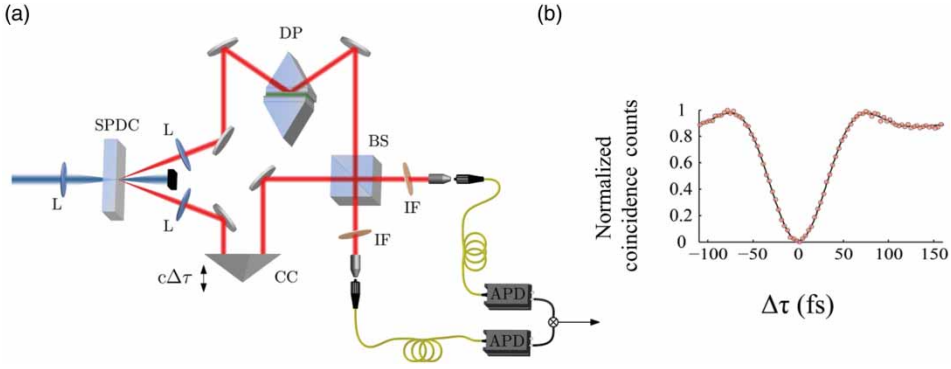

Figure 30. (a) Experimental set up for measuring reflection delay in FTIR with a Hong–Ou–Mandel interferometer. PDC is the parametric downconversion crystal for entangled photon generation, CC is a corner cube retroreflector on a motorized translation stage, BS is a nonpolarizing 50/50 beamsplitter, IF are 10-nm bandpass interference filters centered at 727.6 nm, APD are avalanche photodiode single-photon counting modules. (b) Example data trace containing a Hong–Ou–Mandel dip, along with a numerical fit.

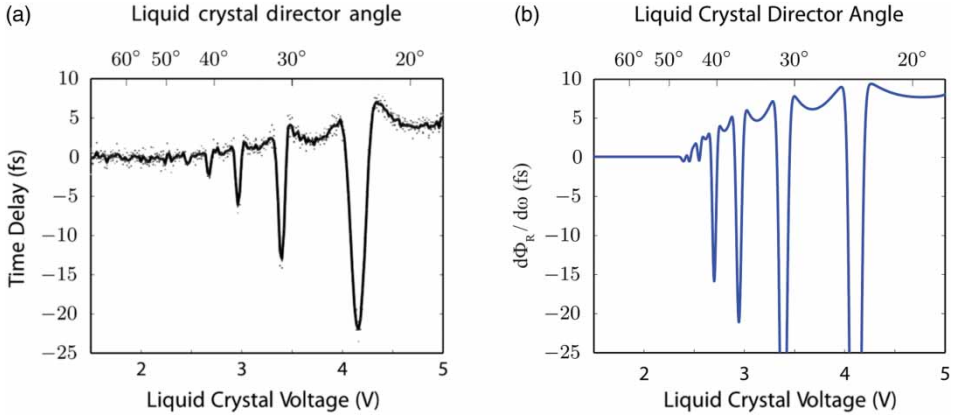

Figure 31. (a) Reflection delay in FTIR from the double-prism structure. The black line is the arithmetic mean of four individual data-sets. Each data point represents an individual Hong–Ou–Mandel trace with 102 seconds of integration time. (b) Predicted $d\phi_R/d\omega$ for 727-nm light propagating through an 8-μm LC cell. (Reproduced with permission [41]).

expected group delay calculated numerically. The experimental data are in excellent agreement with the model predictions.

Two distinct regimes discussed in Section 3.1 are observed (Figure 31). For voltages above approximately 2.2 V, Fabry-Pérot resonances are observed (Figure 31(a)). The black line is the arithmetic mean of four individual data-sets. Each data point represents an individual Hong–Ou–Mandel trace with 102 seconds of integration time. Figure 31(b) shows predicted by simulation $d\phi_R/d\omega$ for 727-nm light propagating through an 8-μm LC cell. Note that the sharp dips on resonance arise from the interference of the Gaussian beam k-vector distribution.

The delay in the tunneling region (below approximately 2.2 V) appears to be identically zero within the experimental uncertainty, observed to be approximately ±1 fs or less, confirming that the Goos–Hänchen contribution is suppressed in this type of measurement. Measurements below 1.5 V were consistent with these results as well, though they have been omitted from the plot for clarity.

In contrast with mechanically tuned double-prism systems, in which the deleterious effects of stress-induced birefringence must be taken into account, our structure has no moving parts and introduces no significant beam deviations during the tunneling process. This has enabled us to experimentally measure the time delay experienced by single photons upon FTIR with sub-fs precision.

These results strongly support a cavity interpretation of the tunneling process. Moreover, our experiments confirm our earlier prediction [40] that the Goos–Hänchen contribution is suppressed in the measurable portion of tunneling delay in this geometry, which may prove important for the fabrication of optical analogs to the tunnel junction and other photonic devices.[82–84]

4. Conclusion

We outlined here our results on applications of thermotropic LCs in quantum science and quantum engineering, in particular in experiments with single (antibunched) and entangled photons. Planar-aligned cholesteric and nematic LC hosts (both monomeric and glassy oligomers) doped with single emitters provide definite linear or circular polarizations of single photons. If the photon has

unknown polarization, filtering it through a polarizer to produce the desired polarization for quantum key distribution with bits based on polarization states of photons, will reduce by half the efficiency of a quantum cryptography system. Cholesteric 1-D photonic bandgap microcavities widely used in cholesteric microlasers can compete with nanostructured microcavities in single-photon count rate enhancement. Much more sophisticated and expensive techniques of high-precision electron beam lithography and focused ion beam lithography for nanostructured microcavities preparation very often do not produce room temperature devices with performances better than SPSs with CLC microcavities. LC microcavities can be tuned by the temperature and electric field providing tunability of SPSs. In future development of this technology, we see hybrid structures of nanoplasmonic/cholesteric-liquid-crystal-microcavity doped with stable, unbleachable single emitters, for example, nanodiamonds with new Si-vacancy color centers (∼0.9 ns fluorescence lifetimes and several nanometers linewidth) or nanocrystals with trivalent rare-earth ions using allowed transitions with nanosecond fluorescence lifetimes.

We also described in this paper, a method of time delay measurements with fs precision using entangled photons in a Hong–Ou–Mandel interferometer. We have presented a double-prism structure under frustrated-total-internal reflection conditions that, with the aid of an electrically tunable nematic LC cell, effectively simulates a quantum mechanical barrier of variable height. Using the same method with a Hong–Ou–Mandel interferometer, our results will be published elsewhere on a tunneling time along a cholesteric photonic bandgap for two different circular polarization components.

Acknowledgements

We acknowledge the assistance of A. Schmid, K. Marshall, J. Winkler, R. Knox, P. Freivald, and C. Supranowitz in some reported experiments and discussions of results with L. Novotny, A. Lieb, and C. Stroud. We used confocal microscope imaging software written by A. Lieb. Some liquid crystal materials were prepared by a S.-H. Chen's group and some single emitters – by T. Krauss' group. Some experiments were carried out at the liquid-crystal clean room and nanometrology facilities at the Laboratory for Laser Energetics, University of Rochester. S.G.L. was supported by the US ARO (Grant No DAAD19-02-1-0285), NSF (Grants No. ECS-0420888, DUE-0633621, DUE- 0920500, EEC-1343673). R.W.B. was supported for this work by the US Defense Threat Reduction Agency–Joint Science and Technology Office for Chemical and Biological Defense (Grant No. HDTRA1-10-1-0025) and by the Canada Excellence Research Chairs Program. L.J.B. was supported by the Air-Force SMART Fellowship.

References

[1] Jacobs SD, Cerqua KA, Marshal KL, Schmid AW, Guardalben MJ, Skerrett KJ. Liquid-crystal laser optics: design, fabrication, and performance. JOSA B. 1988;5:1962–1979.

[2] Schmid A, Papernov S, Li Z-W, Marshal K, Gunderman T, Lee J-C, Guardalben MJ, Jacobs SD. Liquid-crystal materials for high peak-power laser applications. Mol Cryst Liq Cryst. 1991;207:33–42.

[3] Jacobs SD, Marshal KL, Schmid A. Section 14. Liquid Crystals. In: Weber MJ, editor. Handbook of laser science and technology, supplement 2: optical materials. Boca Raton, FL: CRC Press; 1995. p. 509–577.

[4] Lukishova SG, Belyaev SV, Lebedev KS, Magulariya EA, Schmid AW, Malimonenko NV. Behaviour of nonlinear liquid-crystal mirrors, made of a nonabsorbing cholesteric, in the cavity of an YAG:Nd laser operating in the cw regime and at a high pulse repetition frequency. Kvantovaya Elektronika. 1996;23:817–819.

[5] Lukishova SG, Belyaev SV, Lebedev KS, Magulariya EA, Schmid AW, Malimonenko NV. Behaviour of nonlinear liquid-crystal mirrors, made of a nonabsorbing cholesteric, in the cavity of an Nd: YAG laser operating in the cw regime and at a high pulse repetition frequency. Quantum Electron. 1996;26:796–798.

[6] Lukishova SG. Nonlinear optical response of cyanobiphenyl liquid crystals to high-power, nanosecond laser radiation. J Nonlinear Opt Phys Mater. 2000;9(3):365–411.

[7] Khoo I-C. Liquid crystals, physical properties and nonlinear optical phenomena. New York: John Wiley & Sons; 1995.

[8] Khoo I-C, Wu S-T. Optics and nonlinear optics of liquid crystals. Singapore: World Scientific; 1993.

[9] Il'chishin I, Tikhonov E, Tishchenko V, Shpak M. Generation of a tunable radiation by impurity cholesteric liquid crystals. JETP Lett. 1978;32:24–27.

[10] Kopp VI, Fan B, Vithana HKM, Genack AZ. Low-threshold lasing at the edge of a photonic stop band in cholesteric liquid crystals. Opt Lett. 1998;23:1707–1709.

[11] Palffy-Muhoray P, Cao W, Moreira M, Taheri B, Munoz A. Photonics and lasing in liquid crystal materials. Philos Trans A Math Phys Eng Sci. 2006;364:2747–2761.

[12] Coles H, Morris S. Liquid-crystal lasers. Nat Photonics. 2010;4:676–685.

[13] Blinov LM, Bartolino R, editors. Liquid crystal microlasers. Trivandrum: Transworld Research Network; 2010.

[14] Chilaya G, Chanishvili A, Petriashvili G, Barberi R, De Santo MP, Matranga MA. Different approaches of employing cholesteric liquid crystals in dye lasers. Scient Res Mater Sci and Appl. 2011;2:116–129.

[15] Dolgaleva K, Wei SKH, Lukishova SG, Chen, S-H, Schwertz K, Boyd RW. Enhanced laser performance of cholesteric liquid crystals doped with oligofluorene dye. JOSA B. 2008;25:1496–1504.

[16] Shibaev PV, Kopp VI, Genack AZ, Hanelt E. Lasing from chiral photonic band gap materials based on cholesteric glasses. Liq Cryst. 2003;30:1391–1400.

[17] Wei SKH, Chen SH, Dolgaleva K, Lukishova SG, Boyd RW. Robust organic lasers comprising glassy-cholesteric pentafluorene doped with a red-emitting oligofluorene. Appl Phys Lett. 2009;94:Article no. 041111.

[18] Marrucci L, Manzo C, Paparo D. Optical spin-to-orbital angular momentum conversion in inhomogeneous anisotropic media. Phys Rev Lett. 2006;96:Article no. 163905.

[19] Marrucci L, Manzo C, Paparo D. Pancharatnam-Berry phase optical elements for wave front shaping in the visible domain: switchable helical mode generation. Appl Phys Lett. 2006;88:Article no. 221102.

[20] Slussarenko S, Murauski A, Du T, Chigrinov V, Marrucci L, Santamato E. Tunable liquid crystal q-plates with arbitrary topological charge. Opt Express. 2011;19(2):4085–4090.

[21] Anoop KK, Rubano A, Fittipaldi R, Wang X, Paparo D, Vecchione A, Marrucci L, Bruzzese R, Amoruso S. Femtosecond laser surface structuring of silicon using optical vortex beams generated by a q-plate. Appl Phys Lett. 2014;104:Article no. 241604.
[22] Rumala YS, Milione G, Nguyen TA, Pratavieira S, Hossain Z, Nolan D, Slussarenko S, Karimi E, Marrucci L, Alfano RR. Tunable supercontinuum light vector vortex beam generator using a q-plate. Opt Lett. 2013;38:5083–5086.
[23] D'Ambrosio V, Spagnolo N, Del Re L, Slussarenko S, Li Y, Kwek LC, Marrucci L, Walborn SP, Aolita L, Sciarrino F. Photonic polarization gears for ultra-sensitive angular measurements. Nat Comm. 2013;4:Article no. 2432.
[24] Marrucci L. The q-plate and its future. J Nanophoton. 2013;7:Article no. 078598.
[25] Wilkinson TD, Rajesekharan R. Chapter 17. Liquid crystals for nanophotonics. In: Li Q, editor. Liquid crystals beyond displays: chemistry, physics, and applications. Hoboken, NJ: John Wiley & Sons; 2012. p. 525–567.
[26] Diaz A, Khoo I-C. Chapter 3.08. Liquid crystalline nanostructured optical metamaterials. In: Andrews D, Scholes G, Wiederrecht G, editors. Comprehensive nanoscience and technology, vol. 3. London: Elsevier; 2011. p. 225–261.
[27] Si G, Zhao Y, Leong ESP, Liu YJ. Liquid-crystal-enabled active plasmonics: a review. Materials. 2014;7:1296–1317.
[28] Lukishova SG, Schmid AW, McNamara AJ, Boyd RW, Stroud CR. Room temperature single-photon source: single-dye molecule fluorescencein liquid crystal host. IEEE J Sel Top Quantum Electron. 2003;9(6):1512–1518.
[29] Lukishova SG, Bissell LJ, Winkler J, Stroud CR. Resonance in quantum dot fluorescence in a photonic bandgap liquidcrystal host. Opt Lett. 2012;37(7):1259–1261.
[30] Lukishova SG, Schmid AW, Supranowitz CM, Lippa N, McNamara AJ, Boyd RW, Stroud CR. Dye-doped cholesteric-liquid-crystal room-temperature single-photon source. J Mod Opt. 2004;51(9–10):1535–1547.
[31] Lukishova SG, Schmid AW, Knox RP, Freivald P, McNamara A, Boyd RW, Stroud CR, Marshall KL. Single-photon source for quantum information based on single dyemolecule fluorescence in liquid crystal host. Mol Cryst Liq Cryst. 2006;454:403–416.
[32] Lukishova SG, Bissell LJ, Menon VM, Valappil N, Hahn MA, Evans CM, Zimmerman B, Krauss TD, Stroud CR, Boyd RW. Organic photonic bandgap microcavities doped with semiconductor nanocrystals for room-temperature on-demand single-photon sources. J Mod Opt. 2009;56(2 & 3):167–174.
[33] Lukishova SG, Bissell LJ, Stroud CR, Boyd RW. Room temperature single photon sources with definite circular and linear polarizations. Opt Spectrosc. 2010;108(3): 417–424.
[34] Lukishova SG, Schmid AW, Knox R, Freivald P, Bissell L, Boyd RW, Stroud CR, Marshall KL. Room temperature source of single photons of definite polarization. J Mod Opt. 2007;54(2 & 3):417–429.
[35] Lukishova SG, Schmid AW. Near-field optical microscopy of defects in cholesteric oligomeric liquid crystal films. Mol Cryst Liq Cryst. 2006;454:15–21.
[36] Lukishova SG. Liquid crystals under two extremes: (1) high-power laser irradiation, and (2) single-photon level. Mol Cryst Liq Cryst. 2012;559:127–157.
[37] Lukishova SG, Winkler JM, Bissell LJ. Quantum dot fluorescence in photonic bandgap glassy cholesteric liquid crystal structures: microcavity resonance under CW-excitation, antibunching and decay time. Mol Cryst Liq Cryst. 2014; 595(1):98–105. doi:10.1080/15421406.2014.917795.
[38] Lukishova SG, Boyd RW. Efficient room-temperature source of polarized single photons. Stroud. US Patent 7,253,871. 2007 Aug 7.
[39] Bissell LJ. Experimental realization of efficient, room-temperature single-photon sources with definite circular and linear polarizations [dissertation]. Rochester, NY: University of Rochester; 2011.
[40] Gehring GM, Liapis AC, Boyd RW. Tunneling delays in frustrated total internal reflection. Phys Rev A. 2012;85(3):Article no. 032122.
[41] Gehring GM, Liapis AC, Lukishova SG, Boyd RW. Time-domain measurements of reflection delay in frustrated total internal reflection. Phys Rev Lett. 2013;111(3):Article no. 030404.
[42] Liapis AC, Gehring GM, Lukishova SG, Boyd RW. Simulating quantum-mechanical barrier tunneling phenomena with a nematic-liquid-crystal-filled double-prism structure. Mol Cryst Liq Cryst. 2014;592(1):136–143. doi:10.1080/15421406.2014.918084.
[43] Nagali E, Sansoni L, Sciarrino, De Martini F, Marrucci L, Piccirillo B, Karimi E, Santamato E. Optimal quantum cloning of orbital angular momentum photon qubits through Hong–Ou–Mandel coalescence. Nat Photonics. 2009;3:720–723.
[44] Nagali E, Sciarrino F, De Martini F, Marrucci L, Piccirillo B, Karimi E, Santamato E. Quantum information transfer from spin to orbital angular momentum of photons. Phys Rev Lett. 2009;103:Article no. 013601.
[45] Gisin N, Thew R. Quantum communication. Nat Photonics. 2007;1:165–171.
[46] Eisaman MD, Fan J, Migdall A, Polyakov SV. Invited review article: single-photon sources and detectors. Rev Sci Instrum. 2011;82:071101-1–25.
[47] Yamamoto Y, Santori C, Solomon G, Vuckovic J, Fattal D, Waks E, Diamanti E. Single photons for quantum information systems. Prog Inform. 2005;1(1):5–37.
[48] Buckley S, Kelley Rivoire K, Vuckovic J. Engineered quantum dot single-photon sources. Rep Prog Phys. 2012;75:126503-1–27.
[49] Lounis B, Orrit M. Single-photon sources. Rep Prog Phys. 2005;68:1129–1179.
[50] De Vittorio M, Pisanello F, Martiradonna L, Qualtieri A, Stomeo T, Bramati A, Cingolani R. Recent advances on single photon sources based on single colloidalnanocrystals. Opto-Electron Rev (Springer). 2010;18(1):1–9.
[51] Santori C, Fattal D, Yamamoto Y. Single-photon devices and applications. Weinheim: Wiley; 2010.
[52] Lukishova SG. Single photon sources for secure quantum communication. Proc SPIE. 2013;9065:90650C. doi:10.1117/12.2053173.
[53] Kimble HJ, Dagenais M, Mandel L. Photon antibunching in resonance fluorescence. Phys Rev Lett. 1977;39:691–695.
[54] Yamamoto Y. Quantum optics and measurements, AP387. Stanford University; 2011 [cited 2014 Sep 1]. Available from: http://web.stanford.edu/~rsasaki/AP387/AP387.html.
[55] Mandel L, Wolf E. Optical coherence and quantum optics. New York, NY: Cambridge University Press; 1995.
[56] Bennett CH, Brassard G. Quantum cryptography: public key distribution and coin tossing. In: Proceedings of the IEEE international conference on computers, systems, and signal processing. Bangalore, India; 1984. p. 175–179 [cited 2014 Sep 9]. Available from: http://researcher.watson.ibm.com/researcher/files/us-bennetc/BB84highest.pdf.
[57] Gisin N, Ribordy G, Tittel W, Zbinden H. Quantum cryptography. Rev Mod Phys. 2002;74:145–195.

[58] Choi C. MIT technology review; 2013. [cited 2014 Sep 5]. Available from: http://www.technologyreview.com/news/514846/google-and-nasa-launch-quantum-computing-ai-lab/
[59] Ronnow TF, Wang Z, Job J, Boixo S, Isakov SV, Wecker D, Martinis JM, Lidar DA, Troyer M. Defining and detecting quantum speedup. Science. 2014;345:420–424.
[60] Knill E, Laflamme R, Milburn GJ. A scheme for efficient quantum computation with linear optics. Nature. 2001;409:46–52.
[61] Novotny L, Hecht B. Principles of nano-optics. Cambridge, NY: Cambridge University Press; 2012.
[62] Purcell EM. Spontaneous emission at radio frequencies. Phys Rev. 1946;69:681.
[63] Lukishova SG, Winkler JL, Bissell LJ, Mihaylova D, Liapis A, Shi Z, Goldberg D, Menon VM, Boyd R, Chen G, Prasad N. Room-temperature single photon sources based on nanocrystals in photonic/plasmonic nanostructures. Proceeding of SPIE 9254 [cited 2014 Sep 11]. Available from: http://spie.org/Publications/Proceedings/Paper/10.1117/12.2066979
[64] Hong CK, Ou ZY, Mandel L. Measurement of subpicosecond time intervals between two photons by interference. Phys Rev Lett. 1987;59:2044–2046.
[65] Klyshko DN. Photons and nonlinear optics. New York: Gordon and Breach; 1988.
[66] Shih YH, Alley CO. New type of Einstein-Podolsky-Rosen-Bohm experiment using pairs of light quanta produced by optical parametric down conversion. Phys Rev Lett. 1988;61:2921–2924.
[67] Ghosh R, Mandel L. Observation of nonclassical effects in the interference of two photons. Phys Rev Lett. 1987;59:1903–1905.
[68] Kwiat P, Mattle K, Weinfurter H, Zeilinger A, Sergienko AV, Shih YH. New high-intensity source of polarization-entangled photon pairs. Phys Rev Lett. 1995;75(24):4337–4341.
[69] Kwiat PG, Waks E, White AG, Appelbaum I, Eberhard PH. Ultrabright source of polarization-entangled photons. Phys Rev A. 1999;60:R773–R776.
[70] Winful HG, Zhang C. Tunneling delay time in frustrated total internal reflection. Phys Rev A. 2009;79(2):Article no. 023826.
[71] Papoular DJ, Clade P, Polyakov SV, Migdall A, Lett PD, Phillips WD. Measuring optical tunneling times using a Hong-Ou-Mandel interferometer. Opt Express. 2008;16:16005–16012.
[72] Wigner EP. Lower limit for the energy derivative of the scattering phase shift. Phys Rev. 1955;98(1):145–147.
[73] Winful HG. Tunneling time, the Hartman effect, and superluminality: a proposed resolution of an old paradox. Phys Rep. 2006;436:1–69.
[74] Pieranski P. Classroom experiments with chiral liquid crystals. In: Kitzerow H-S, Bahr C, editors. Chirality in liquid crystals. New York: Springer; 2001. p. 28–66.
[75] Bunning TJ, Kreuzer F-H. Cyclosiloxane-based liquid crystalline materials. Trends Polym Sci. 1995;3:318–323.
[76] Goos F, Hänchen H. Ein neuer und fundamentaler versuch zur totalreflexion. Ann Phys. 1947;436(7–8):333–346.
[77] Merano M, Aiello A, Hooft GW, van Exter MP, Eliel ER, Woerdman JP. Observation of Goos-Hänchen shifts in metallic reflection. Opt Express. 2007;15:15928–15934.
[78] Geary JM, Goodby JW, Kmetz AR, Patel JS. The mechanism of polymer alignment of liquid-crystal materials. J Appl Phys. 1987;62(10):4100–4108.
[79] Berreman DW. Optics in stratified and anisotropic media: 4 × 4-matrix formulation. J Opt Soc Am. 1972;62(1):502–510.
[80] Wu S-T, Efron U, Hess LD. Birefringence measurements of liquid crystals. Appl Opt. 1984;23:3911–3915.
[81] Steinberg AM, Kwiat PG, Chiao RY. Measurement of the single-photon tunneling time. Phys Rev Lett. 1993;71:708–711.
[82] Lukishova SG, Pashinin PP, Batygov SK, Arkhangelskaya VA, Poletimov AE, Scheulin AS, Terentiev BM. High-power laser-beam shaping using apodized apertures. Laser Part Beams. 1990;8(1–2):349–360.
[83] Jian AQ, Zhang XM. Resonant optical tunneling effect: recent progress in modeling and applications. IEEE J Sel Top Quantum Electron. 2013;19(3):Article no. 9000310.
[84] Sun DG. A proposal for digital electro-optic switches with free-carrier dispersion effect and Goos-Hanchen shift in silicon-on-insulator waveguide corner mirror. J Appl Phys. 2013;114:Article no. 104502.